Physiol Genomics 18: 232–244, 2004.
First published April 27, 2004; 10.1152/physiolgenomics.00026.2004.

Comprehensive transthoracic cardiac imaging in mice using ultrasound biomicroscopy with anatomical confirmation by magnetic resonance imaging

Yu-Qing Zhou,[1] F. Stuart Foster,[1,2,3] Brian J. Nieman,[1] Lorinda Davidson,[1] X. Josette Chen,[1,3] and R. Mark Henkelman[1,2,3]

[1]*Mouse Imaging Centre at Hospital for Sick Children,* [2]*Sunnybrook and Women's College Health Sciences Centre and* [3]*Departments of Medical Biophysics of the University of Toronto, Toronto, Ontario, Canada M5G 1X8*

Submitted 7 February 2004; accepted in final form 22 April 2004

Zhou, Yu-Qing, F. Stuart Foster, Brian J. Nieman, Lorinda Davidson, X. Josette Chen, and R. Mark Henkelman. Comprehensive transthoracic cardiac imaging in mice using ultrasound biomicroscopy with anatomical confirmation by magnetic resonance imaging. *Physiol Genomics* 18: 232–244, 2004. First published April 27, 2004; 10.1152/physiolgenomics.00026.2004.—High-frequency ultrasound biomicroscopy (UBM) has recently emerged as a high-resolution means of phenotyping genetically altered mice and has great potential to evaluate the cardiac morphology and hemodynamics of mouse mutants. However, there is no standard procedure of in vivo transthoracic cardiac imaging using UBM to comprehensively phenotype the adult mice. In this paper, the characteristic mouse thoracic anatomy is elucidated using magnetic resonance (MR) imaging on fixed mice. Besides the left parasternal and apical windows commonly used for transthoracic ultrasound cardiac imaging, a very useful right parasternal window is found. We present strategies for optimal visualization using UBM of key cardiac structures including: *1*) the right atrial inflow channels such as the right superior vena cava; *2*) the right ventricular inflow tract via the tricuspid orifice; *3*) the right ventricular outflow tract to the main pulmonary artery; *4*) the left atrial inflow channel, e.g., pulmonary vein; *5*) the left ventricular inflow tract via the mitral orifice; *6*) the left ventricular outflow tract to the ascending aorta; *7*) the left coronary artery; and *8*) the aortic arch and associated branches. Two-dimensional ultrasound images of these cardiac regions are correlated to similar sections in the three-dimensional MR data set to verify anatomical details of the in vivo UBM imaging. Dimensions of the left ventricle and ascending aorta are measured by M-mode. Flow velocities are recorded using Doppler at six representative intracardiac locations: right superior vena cava, tricuspid orifice, main pulmonary artery, pulmonary vein, mitral orifice, and ascending aorta. The methodologies and baseline measurements of inbred mice provide a useful guide for investigators applying the high-frequency ultrasound imaging to mouse cardiac phenotyping.

cardiovascular morphology; hemodynamics; M-mode; Doppler; phenotyping

A VARIETY OF NONINVASIVE IMAGING technologies have been developed for phenotyping the genetically engineered adult mice created to model human diseases (1, 14, 16, 17, 24). Of these technologies, ultrasound imaging is increasingly being used for characterizing phenotypes of the cardiovascular system in mutant and transgenic mouse models, because of its inherent advantages such as quick and real-time imaging, low cost, and most importantly the possibility of obtaining the structural, functional, and hemodynamic information (5, 7).

Conventional clinical ultrasound systems with imaging frequency up to 15 MHz have been used for cardiac observation on mice. With two-dimensional (2D) and M-mode imaging, the left ventricular dimensions have been measured. Following the formulas established in human echocardiography, the left ventricular systolic function parameters and left ventricular mass have been calculated (6, 15, 21, 25, 31, 34). Aortic flow velocity measured using Doppler, along with the aortic diameter measured by 2D imaging or M-mode, has been used for assessing the cardiac output (34). The Doppler mitral inflow pattern has been recorded for evaluating left ventricular diastolic function (15, 25, 31). However, the limited spatial resolution of the 2D imaging (~250 μm laterally and ~100 μm axially at 15 MHz) is not ideal for visualizing the small cardiac structures of mice (35). For this reason, many important regions of the mouse heart other than the left ventricle and aortic root have not yet been explored. Considering that phenotypes caused by gene manipulation may involve all elements of the heart, it is essential to study the entire heart in order to fully characterize cardiac phenotypes in any newly created mutant mice.

Recent advances in high-frequency ultrasound imaging, commonly referred to as ultrasound biomicroscopy (UBM), provide great potential for more extensive exploration on the mouse heart (11, 12, 22). In a previous study, the frequency range from 20 to 40 MHz was found suitable for the cardiac imaging in adult mice with good spatial resolution and adequate penetration (35). However, a systematic methodology for in vivo transthoracic cardiac imaging using UBM in the adult mouse is still lacking.

To establish such a methodology for the first time on mice, the thoracic gross anatomy has to be evaluated, and more importantly the individual structures in the ultrasound 2D images need to be identified. Whole body three-dimensional (3D) magnetic resonance (MR) imaging of a fixed mouse provides excellent visualization of internal anatomy (18, 19) and clearly delineates the morphology of the thoracic organs such as lung lobes, heart, vessels, and their in situ spatial relations (37). The 3D MR data set can be used for the observation of structural continuity, and selected MR sections provide comparative anatomy for the corresponding UBM images.

Using a newly developed UBM with a transducer frequency of 30 MHz, this study was conducted on inbred C57BL/6 adult mice for the following purposes: *1*) to explore all possible acoustical windows for transthoracic cardiac ultrasound imaging; *2*) to define ultrasound imaging sections suitable for cardiac structural, functional, and Doppler hemodynamic evaluations; *3*) to identify the individual anatomical structures in

Article published online before print. See web site for date of publication (http://physiolgenomics.physiology.org).

Address for reprint requests and other correspondence: Y.-Q. Zhou, Mouse Imaging Centre, The Hospital for Sick Children, 555 Univ. Ave., Toronto, Ontario, Canada M5G 1X8 (E-mail: yqzhou@sickkids.ca).

ultrasound 2D images with comparative MR images; and *4*) to measure the dimensions of key cardiac structures and the Doppler flow parameters at representative intracardiac sites by in vivo ultrasound imaging.

MATERIALS AND METHODS

Experimental protocol was approved by the Animal Care Committee of the Hospital for Sick Children in Toronto, and the study was conducted in accordance with guidelines established by the Canadian Council on Animal Care.

In Vivo Transthoracic Cardiac Imaging Using UBM

Mice. Seventeen inbred C57BL/6 adult mice were studied (5 males and 12 females; age range, 5–9 wk; body wt, 20 ± 1 g) (Charles River Laboratories, Wilmington, MA).

UBM specifications. A newly developed UBM (Vevo 660; VisualSonics, Toronto, Ontario) was used in the current study. The single-crystal mechanical transducer has a central frequency of 30 MHz, a focal length of 12.7 mm, and a frame rate of 30 Hz. The maximum field of view of 2D imaging is 20 × 20 mm with spatial resolution of ~115 μm (lateral) by ~55 μm (axial). In M-mode, the repetition rate is 1,000 Hz, with 512 depth samples for an 8-mm sampling window. The Doppler pulse repetition frequency is up to 96 kHz, corresponding to a maximum unaliased velocity of 120 cm/s (with incidence angle being zero). This range of velocity measurement can be doubled by shifting the baseline. In this study the axial dimension of Doppler sample volume was ~0.5 mm.

Animal preparation. Mice were anesthetized using 1.5% isoflurane and laid supine on a platform with all legs taped to ECG electrodes for heart rate monitoring. Body temperature was monitored via a rectal thermometer (Indus Instruments, Houston, TX) and maintained at 36–38°C using a heating pad and lamp (Fig. 1). All hair was removed from the chest using a chemical hair remover (Nair; Carter-Horner, Mississauga, Ontario). The inlet and inferior boundary of the thorax were marked, and the midline of the chest was drawn and divided into three equal segments. We define the terms for the transducer orientation relative to mouse as superior, inferior, anterior, and posterior, which correspond to the cranial, caudal, ventral, and dorsal aspects of the mouse body, respectively (Fig. 1*A*). The configuration of the 2D imaging plane is shown in Fig. 1*B*. Three orthogonal planes of the mouse body are illustrated in Fig. 1*C*. To provide a coupling medium for the transducer, a prewarmed ultrasound gel (Aquasonic 100; Parker Laboratories, Orange, NJ) was spread over the chest wall. Imaging commenced after waiting ~1–2 min for the mouse to stabilize.

At first, a pilot observation was conducted in the first five mice to explore possible acoustic windows by sweeping the exploring image plane across the whole chest. Three major windows were found in the right parasternal, left parasternal, and apical regions. After establish-

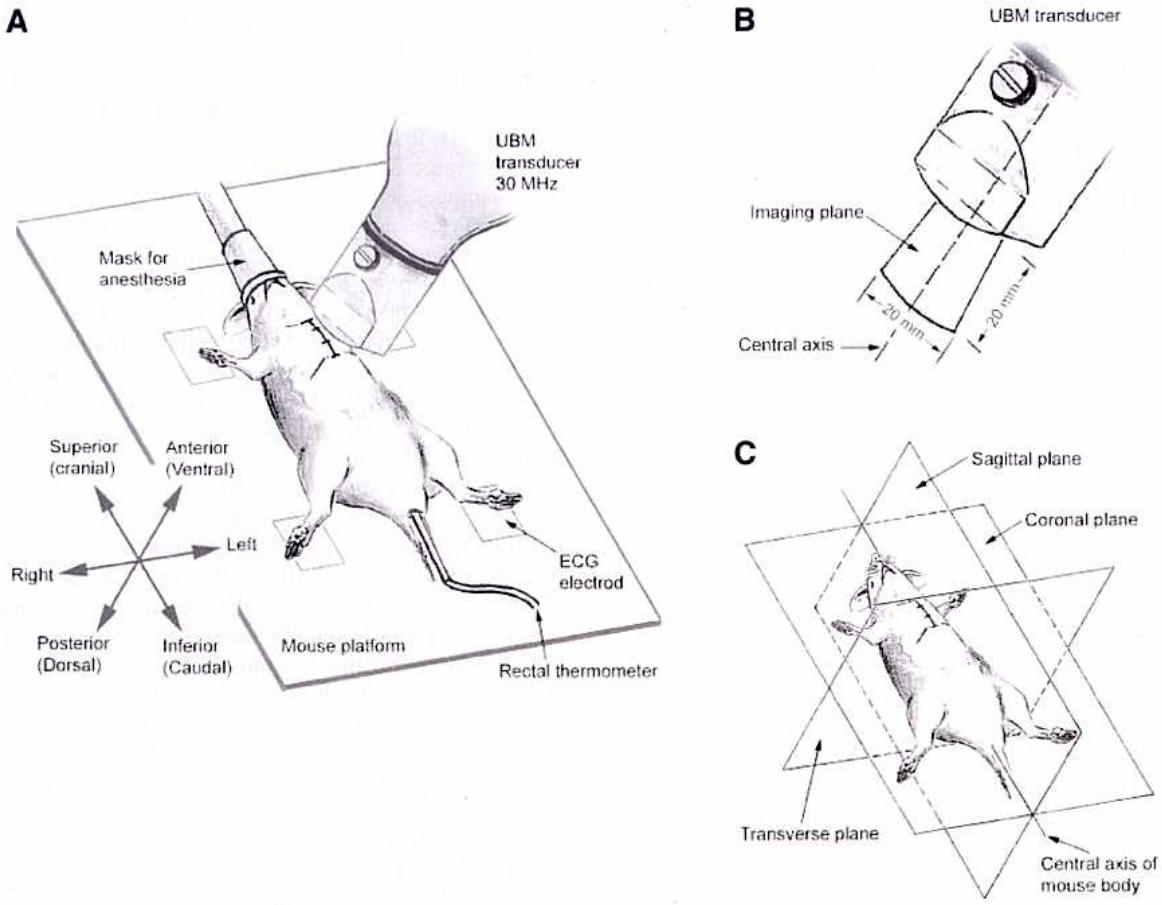

Fig. 1. Sketches of the experimental setup. *A*: the mouse orientation and its spatial relation with the ultrasound biomicroscopy (UBM) transducer. The terms superior, inferior, anterior, and posterior sides correspond to the cranial, caudal, ventral, and dorsal aspects of the mouse body, respectively. The inlet and inferior border of the thorax are marked. The midline of the chest is drawn and divided into three equal parts: the upper, middle and lower one-thirds. *B*: the configuration of two-dimensional (2D) imaging plane of UBM transducer. *C*: the three orthogonal planes of the mouse body.

ing the window, the transducer was carefully oriented for 2D imaging section to visualize specific structures. With the experience from the preliminary study on the first 5 mice, systematic study was conducted in the remaining 12 mice. In each mouse, cardiac imaging was initiated in the upper right parasternal region and went down through the entire right parasternal window to the xiphoid level. Then the left parasternal window and finally the apical window were explored. From each window, the longitudinal and transverse imaging sections were applied. At first, the structure of interest was selected by sweeping the imaging plane within each window. For best visualization of each targeted cardiac structure, the imaging section was optimized by carefully adjusting the transducer location, the direction of its central axis, and the orientation of the imaging plane. The orientation of the finally optimized 2D imaging section was carefully evaluated relative to the three orthogonal planes of the mouse body. M-mode recording was made with the targeted structures such as left ventricular or aortic wall perpendicular to the ultrasound beam. Doppler sampling was made with the smallest incidence angle between the Doppler beam and the assumed blood flow direction in the targeted flow channel. Therefore, for each specific part of the heart, several imaging sections from different windows were identified and used for either M-mode or Doppler recording. The Doppler flow velocity sampling was started in the upper right parasternal region for the aortic flow; continued downward in the right parasternal window

Table 1. *Summary of the representative sections of transthoracic cardiac imaging using UBM in mice*

Code of Section	Location of Transducer	Direction of Transducer Central Axis	Orientation of Imaging Plane	Targeted Structures and Imaging Modality
		Right parasternal longitudinal sections		
RL1	Upper 1/3 of chest	Mainly inferior and posterior, slightly leftward, ~40° with coronal plane	Almost parallel to central axis of mouse body	AAo Doppler flow velocity (Fig. 6, *D* and *E*)
RL2	Upper 1/3 of chest	Mainly posterior, slightly inferior and leftward, ~70° with coronal plane	Parallel to central axis of mouse body	RSVC 2D imaging and Doppler flow velocity (Fig. 3, *A* and *B*)
RL3	Middle 1/3 of chest	Posterior and slightly leftward, ~70° with coronal plane	Parallel to central axis of mouse body	AAo, IA, and RCCA 2D imaging (Fig. 9*C*)
RL4	Middle 1/3 of chest	Leftward and posterior, ~40° with coronal plane	Parallel to central axis of mouse body	Entire AAr and the origins of three branches 2D imaging (Fig. 9*A*)
RL5	Lower 1/3 of chest	Posterior and leftward, ~70° with coronal plane	Parallel to central axis of mouse body	MO, AO, and AAo 2D imaging and M-mode recording of MV, and AV and AAo walls (Fig. 5, *A* and *B*; Fig. 7,*D–G*)
		Right parasternal transverse section		
RT1	Lower 1/3 of chest	Mainly posterior, slightly superior and leftward, ~70° with coronal plane	Rotated counterclockwise from transverse plane by ~30°	RVIT 2D imaging of RA and RV; Doppler flow velocity of TO (Fig. 4, *A* and *B*)
		Left parasternal longitudinal sections		
LL1a	Upper 1/3 of chest	Mainly posterior, slightly rightward, ~70° with coronal plane	Parallel to central axis of mouse body	LCCA (long axis) and AAr (short axis) 2D imaging (Fig. 9*D*)
LL1b	Upper 1/3 of chest	Parallel to LL1a, moved leftward in parallel	Parallel to LL1a, moved leftward in parallel	Proximal LSCA, AAr (short axis), and LSVC 2D imaging (Fig. 9*E*)
LL2	Middle 1/3 of chest	Rightward and posterior, ~40° with coronal plane	Parallel to central axis of mouse body	LVOT, AO, AAo, with RA, RV, RVOT 2D imaging and M-mode recording (Fig. 7, *A* and *B*)
LL3	Middle 1/3 of chest	Posterior and rightward, ~65° with coronal plane	Almost parallel to central axis of mouse body	PO and MPA 2D imaging and Doppler flow velocity (Fig. 6, *A* and *B*)
LL4	Middle to lower 1/3 of chest	Mainly posterior and rightward, slightly inferior, ~70° with coronal plane	Rotated counterclockwise by ~15°	LVIT 2D imaging of LA, MO, LV; M-mode recording of LV; Doppler flow velocity of PV (Fig. 3, *D* and *E*)
		Left parasternal transverse sections		
LT1	Upper 1/3 of chest	Mainly posterior, slightly rightward, ~60° with coronal plane	Parallel to transverse plane	RSVC, IA, LCCA, LSCA, and LSVC in short axes behind thymus 2D imaging
LT2	Middle 1/3 of chest	Mainly posterior, slightly rightward, ~60° with coronal plane	Rotated counterclockwise from transverse plane by ~15°	MPA (long axis) and AO (short axis) 2D imaging and Doppler flow velocity of MPA
LT3	Middle 1/3 of chest	Mainly posterior, slightly rightward, ~70 degrees with coronal plane	Rotated clockwise from transverse plane by ~15°	LCA 2D imaging and Doppler flow velocity (Fig. 8, *A* and *B*)
LT4	Lower 1/3 of chest	Mainly posterior, slightly rightward and inferior, ~70° with coronal plane	Rotated counterclockwise from transverse plane by 15°	LV in short axis 2D imaging and M-mode recording (Fig. 5, *C* and *D*)
			Apical section	
Ap1	Apical region	Superior, rightward and posterior, ~45° with coronal plane	~45 degrees with coronal plane	LA, LV, RA, and RV 2D imaging and Doppler flow velocity of MO and TO (Fig. 4,*D* and *E*)

UBM, ultrasound biomicroscopy; AAo, ascending aorta; AAr, aortic arch; AO, aortic orifice; AV, aortic valve; IA, innominate artery; LA, left atrium; LCA, left coronary artery; LCCA, left common carotid artery; LSCA, left subclavian artery; LSVC, left superior vena cava; LV, left ventricle; LVIT, left ventricular inflow tract; LVOT, left ventricular outflow tract; MO, mitral valvular orifice; MPA, main pulmonary artery; MV, mitral valve; PO, pulmonary orifice; PV, pulmonary vein; RA, right atrium; RCCA, right common carotid artery; RSCA, right subclavian artery; RSVC, right superior vena cava; RV, right ventricle; RVIT, right ventricular inflow tract; RVOT, right ventricular outflow tract; and TO, tricuspid valvular orifice.

for the right superior vena cava flow and tricuspid flow; then conducted in the left parasternal window for the pulmonary arterial flow and pulmonary venous flow; and finally made in the apical window for the mitral flow. The complete examination for each mouse lasted for about 45–60 min. All representative 2D imaging planes, associated transducer orientations, targeted structures, and applied ultrasound imaging modalities are summarized in Table 1.

Measurements and statistical analysis. M-mode recording and Doppler flow velocity spectrum were quantified in the last 12 mice (5 males and 7 females, ages 6–7 wk; body wt = 21 ± 1 g). All measurements were made according to the standards established in human echocardiography (26, 28). The M-mode recordings of the left ventricle in both long-axis view (LL4) and short-axis view (LT4) were analyzed for the ventricular wall thicknesses and chamber diameters. The M-mode recordings of the ascending aorta from the right (RL5) and left (LL2) parasternal longitudinal sections were analyzed for the aortic diameter. The M-mode measurements from three cardiac cycles were averaged. In analyzing the Doppler flow spectra of the right superior vena cava and pulmonary vein, the reverse wave caused by atrial contraction (A wave) was first identified, then the early diastolic wave (D wave, an forward waveform preceding A wave) and the systolic wave (S wave, another forward waveform following A wave) were determined. Because the flow pattern of right superior vena cava changed dramatically with respiration, the cardiac beats at the end of inspiration were excluded from analysis. The peak flow velocity and time-velocity integral were quantified and averaged for five consecutive cardiac cycles. The paired student *t*-tests were used to compare the Doppler parameters between the right and left sides of the heart at the similar anatomical levels. All data is expressed as means ± SE, and statistical significance was chosen as $P < 0.05$.

Whole Body Mouse MR Imaging for Anatomic Confirmation of Ultrasound Imaging

Four mice (2 males and 2 females) from the study group were perfused with gadopentetate dimeglumine (Magnevist, Berlex Canada, Quebec) and fixed by infusing formalin for whole body MR imaging (37). Under the guidance of real-time UBM 2D imaging, a catheter was introduced into the left ventricle of the anesthetized mouse for the perfusion of gadopentetate dimeglumine and formalin. The jugular and femoral veins were cut for draining the blood and perfusate.

MR images were obtained from a 40-cm bore, 7-T magnet (Magnex Scientific, Oxford, UK) controlled by a UnityInova console (Varian NMR Instruments, Palo Alto, CA) as previously described (2). The fixed whole mouse was placed in a 3-cm diameter radiofrequency millipede coil (Varian NMR Instruments) (33). We used a conventional spin echo with the following imaging parameters: 200-ms repetition time, 10-ms echo time, 2.8 × 2.8 × 12-cm field of view, and 420 × 420 × 1,800 imaging matrix providing isotropic voxels of 67 μm. This acquisition required a total imaging time of 9 h, 48 min and achieved a signal-to-noise ratio of ~15 per voxel. After the reconstruction of the raw data, the 3D data set was visualized, processed, and analyzed with Amira software (TGS, San Diego, CA). A series of 2D MR images were selected from the 3D data set approximating the orientation of the UBM in vivo cardiac images. Continuity of the cardiac structures and vascular lumens were investigated by scanning the selected section through the 3D data set to provide definitive identification of the individual structures seen in the corresponding 2D ultrasound images.

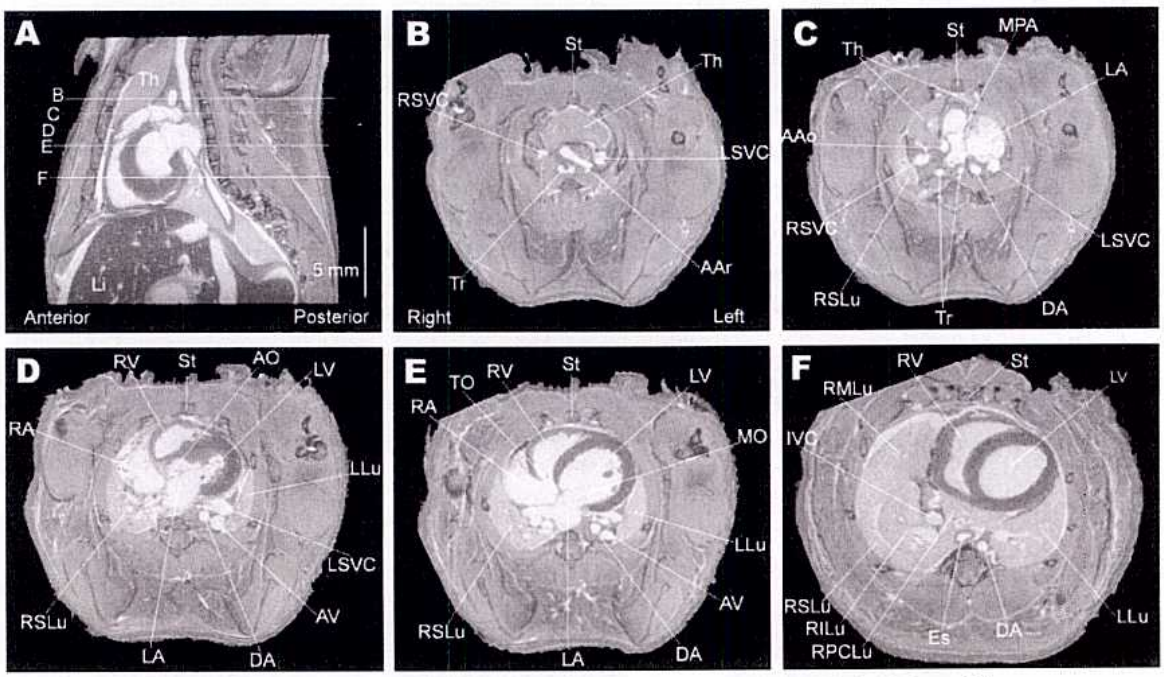

Fig. 2. Magnetic resonance (MR) images of a fixed mouse. *A*: midline sagittal section of the mouse thorax with the horizontal lines indicating the levels of the transverse sections in *B–F*. *B*: the transverse section at the level of the aortic arch (AAr). *C*: the transverse section at the level of the main pulmonary artery (MPA). *D*: the transverse section at the level of the aortic orifice (AO). *E*: the transverse section at the level of the mitral orifice (MO) and tricuspid orifice (TO). *F*: the transverse section at the level of the left (LV) and right ventricles (RV). AAo, ascending aorta; AV, azygos vein; Es, esophagus; DA, descending aorta; IVC, inferior vena cava; LA, left atrium; Li, liver; LLu, left lung; LSVC, left superior vena cava; RA, right atrium; RILu, inferior lobe of the right lung; RMLu, middle lobe of the right lung; RPCLu, postcaval lobe of the right lung; RSLu, superior lobe of the right lung; RSVC, right superior vena cava; St, sternum; Th, thymus; Tr, trachea.

RESULTS

Based on the 3D MR data, the following anatomical characteristics of mouse thorax were identified (Fig. 2) as follows. *1*) The lung lobes are located posteriorly and inferiorly relative to the heart. The top of the right superior lung lobe is below the level of the aortic arch, and the top of left lung is at the level of the main pulmonary artery (Fig. 2, *B–D*). The right lung lobes surround the right heart on the lateral and posterior sides, but the left lung mainly presents on the posterior side of the left heart (Fig. 2, *D–F*). *2*) The sternum is narrow in the transverse section. *3*) A large thymus is located between the sternum and the cardiac base and great vessels and extends laterally far beyond the margins of sternum (Fig. 2, *A–C*). *4*) The aortic orifice and ascending aorta are on the right side of the midline with the mitral orifice located relatively leftward and posteriorly (Fig. 2, *C* and *D*). (5) There is no lung tissue in front of the right and left superior vena cavae, but the inferior vena cava is surrounded by the middle, inferior, and postcaval lobes of the right lung before it enters into the right atrium (Fig. 2, *B*, *C*, and *F*).

All UBM image data are presented in a sequence following the route of the blood flow in the cardiovascular system. The atrial inflow channels are first described, followed by the ventricular inflow tracts via atrioventricular orifices, and then the ventricular outflow tracts to the great arteries. Finally, the coronary artery, the aortic arch, and the associated branches are described. The right and left sides of the heart are compared with each other by placing the 2D images and Doppler flow waveforms obtained at the similar anatomical levels of both sides in the same figure. The representative UBM images are demonstrated in Figs. 3–9. To confirm 2D ultrasound images, MR images of similar sections are shown with the identified individual structures.

The right atrial inflow channels include three vena cavae. The right superior vena cava was most readily visualized by a

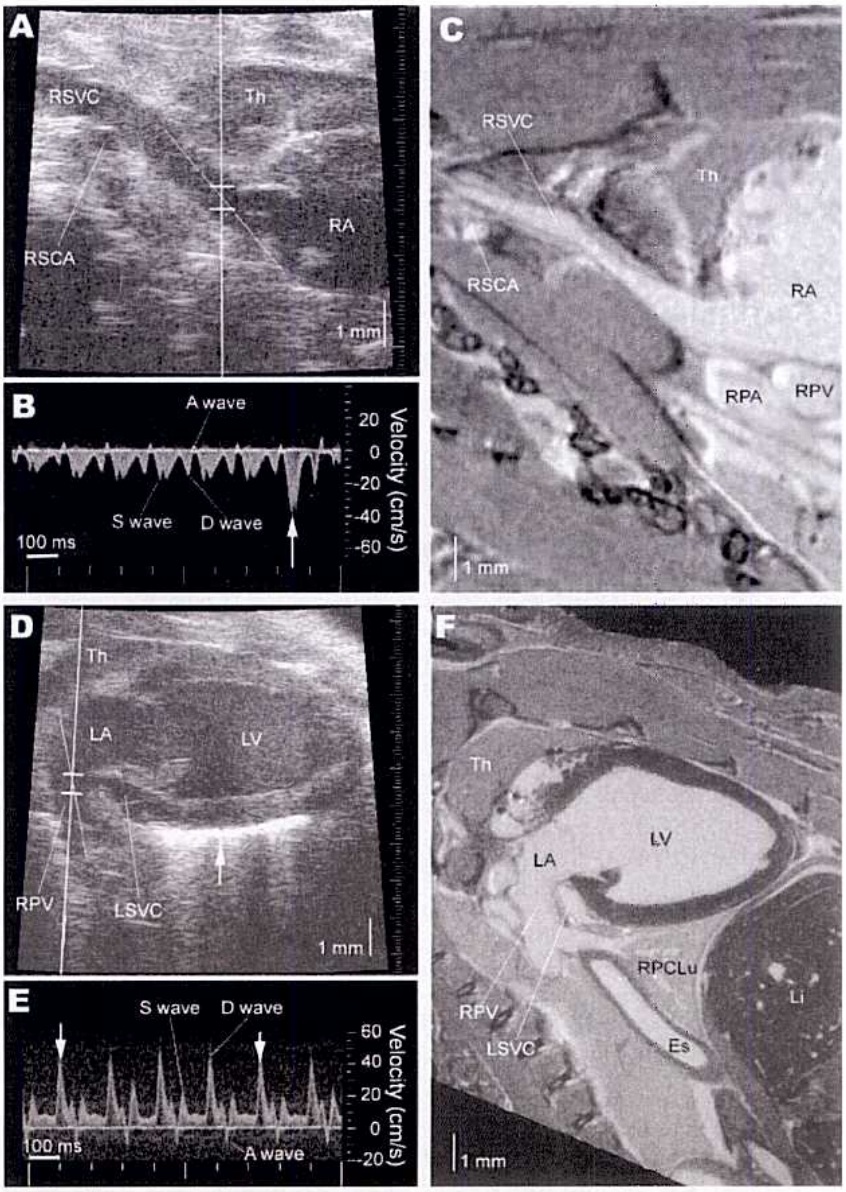

Fig. 3. UBM imaging of the right and left atrial inflow channels, with anatomical confirmation by MR imaging. *A*: UBM image of a right parasternal longitudinal section (RL2) showing the RSVC in its long axis, with Doppler sampling volume at its entrance to RA. *B*: Doppler flow spectrum of RSVC, showing a small retrograde wave caused by atrial contraction during late diastole (A wave), a medium antegrade wave during early diastole (D wave) preceding the A wave, and a relatively higher antegrade wave during systole (S wave) following the A wave. Arrow marks large S wave at the end of inspiration. *C*: MR image of the similar section as for the UBM image in *A*, showing the vascular continuity from RSVC to RA and the surrounding organs such as Th, right subclavian artery (RSCA), right pulmonary artery (RPA), and right pulmonary vein (RPV). *D*: UBM image of a left parasternal longitudinal section (LL4) showing the right pulmonary vein (RPV), LA, and LV, with the Doppler sample volume in the entrance of the RPV to LA. Arrow indicates the bright reverberations at the interface exiting the myocardium into the lung. *E*: the Doppler flow spectrum from the pulmonary vein showing a small retrograde A wave, a higher D wave, and a lower S wave. The arrows indicate heart beats at the end of inspiration. *F*: MR image of the similar section as for UBM image in *D*. Refer to the legends of Figs. 1 and 2 for definitions of other abbreviations.

right parasternal longitudinal section (RL2) (Fig. 3*A*). Its Doppler flow spectrum (Fig. 3*B*) showed a small retrograde A wave, a medium D wave preceding the A wave, and a relatively larger S wave following the A wave. Dramatic increases in the amplitude and change in the shape of the waveforms were observed around the end of inspiration (Fig. 3*B*). The left superior vena cava was also visible in a left parasternal longitudinal section (LL1b), and the Doppler flow spectrum was recordable. The inferior vena cava was viewed in the hepatic segment and below, but its entrance to the right atrium could not be properly imaged because of the acoustical shadowing from the lung lobes.

The left atrial inflow channel, e.g., the pulmonary vein, was readily visible in a left parasternal longitudinal section (LL4) (Fig. 3*D*). The recorded Doppler flow spectrum showed a small retrograde A wave, a considerably higher D wave, and a lower S wave, with slight decrease in D wave during inspiration (Fig. 3*E*).

The right ventricular inflow tract was visible in three sections. In the right parasternal transverse section (RT1), the right atrium, tricuspid orifice, and right ventricle were visualized, often along with the right ventricular outflow tract (Fig. 4*A*). The tricuspid Doppler flow spectrum was readily recordable and showed a lower early diastolic ventricular filling wave (E wave), a higher late diastolic ventricular filling wave due to the atrial contraction (A wave), and considerable increase in the amplitude of waveform during inspiration (Fig. 4*B*). The apical four-chamber view (Ap1) (Fig. 4*D*) provides another option for recording the tricuspid flow. In the longitudinal section from the left parasternal window (LL2), the right atrium and right ventricle were well demonstrated in contrast to the left ventricular outflow tract and ascending aorta (Fig. 7*A*).

The left ventricular inflow tract was well observed in a left parasternal longitudinal section (LL4). The left atrium and ventricle were clearly demonstrated in 2D imaging (Fig. 3*D*). For measuring the left ventricular chamber dimension, wall

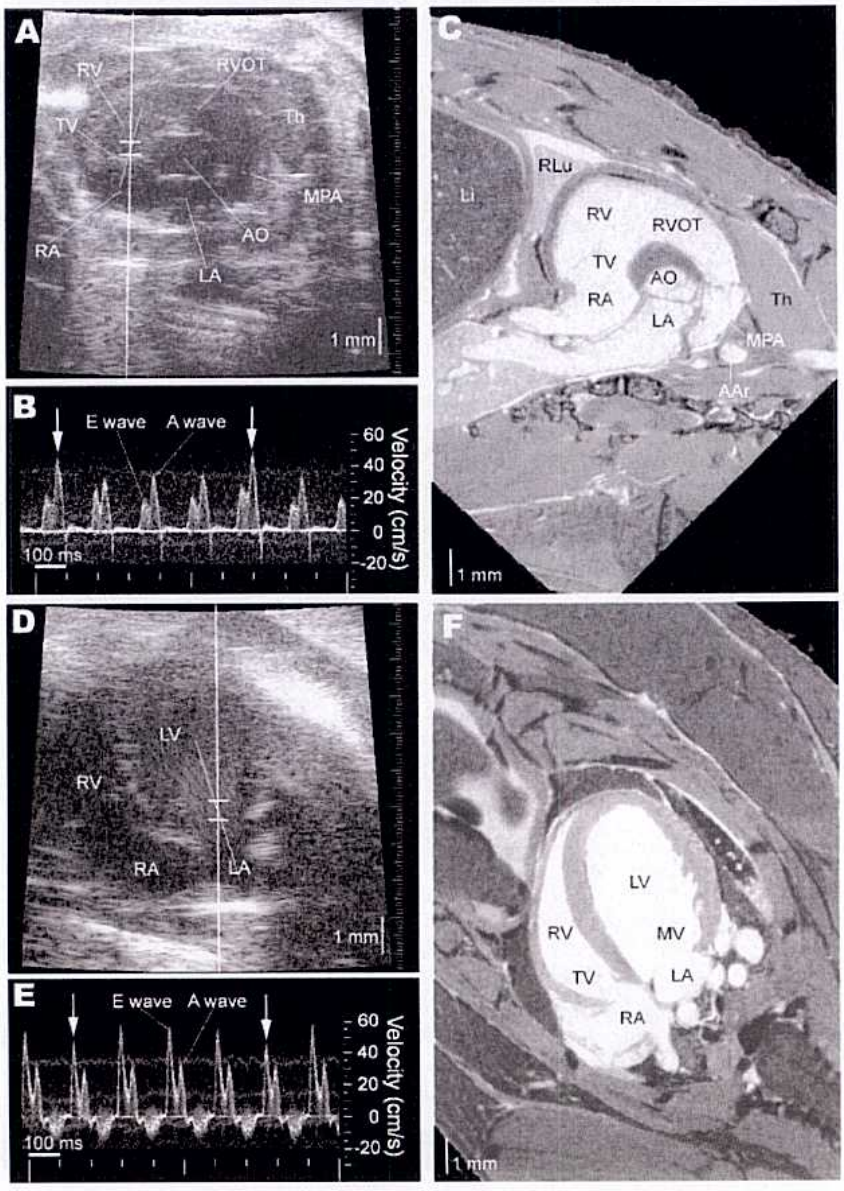

Fig. 4. UBM imaging of the right and left ventricular inflow tracts, with anatomical confirmation by MR imaging. *A*: UBM image of a right parasternal transverse section (RT1) showing the right ventricle inflow tract with the Doppler sample volume at TO. *B*: tricuspid Doppler flow spectrum, showing lower early diastolic ventricular filling waves (E wave) and higher late diastolic ventricular filling waves caused by atrial contraction (A wave). The arrows indicate heart beats at the end of inspiration. *C*: MR image of the similar section as for the UBM image in *A*. *D*: UBM image of a apical four-chamber section (Ap1) showing the left ventricular inflow tract, with Doppler sample volume at MO. *E*: mitral Doppler flow spectrum showing higher E wave and lower A wave. The arrows indicate the heart beats at end of inspiration. *F*: MR image at the similar section as for UBM image in *D*. MV, mitral valve; RLu, right lung; RVOT, right ventricular outflow tract; TV, tricuspid valve. Refer to the legends of Figs. 1–3 for definitions of other abbreviations.

thickness, and systolic function, M-mode was recorded at the tip of the papillary muscle in this view. In the apical four-chamber view (Ap1) (Fig. 4*D*), the mitral Doppler flow spectra was recorded and showed higher E wave and lower A wave, with slight decrease in the amplitude of the waveform during inspiration (Fig. 4*E*). The mitral valve was most easily observed in a longitudinal section from the right parasternal window (RL5), and M-mode trace of the valve movement was recorded (Fig. 5, *A* and *B*). M-mode recording was also made in the short-axis view of the left ventricle from the left parasternal window (LT4) for the ventricular dimension and systolic function (Fig. 5, *C* and *D*).

The right ventricular outflow tract to the main pulmonary artery was observed mainly in two sections. The left parasternal longitudinal section (LL3) visualized the main pulmonary artery located between the left atrium and aortic arch (Fig. 6*A*), and Doppler flow spectrum was recorded with a small incidence angle (Fig. 6*B*). The left parasternal transverse section at the level of the cardiac base (LT2) showed the long-axis view of the main pulmonary artery and two branches, along with the short-axis view of the aortic orifice (data not shown).

The left ventricular outflow tract was followed up to the ascending aorta via aortic orifice. From the upper right parasternal approach (RL1), the Doppler flow spectrum of the ascending aorta was recorded with a small incidence angle (Fig. 6, *D* and *E*). From a left parasternal longitudinal section (LL2), the left ventricular outflow tract and ascending aorta were well visualized in their long axes, along with the right atrium and ventricle located in the far field (Fig. 7*A*). M-mode recording was made for aortic diameter measurement in this view (Fig. 7*B*). The aortic orifice and ascending aorta were more clearly imaged from the right parasternal approach (RL5) (Fig. 7, *D* and *F*). M-mode recording demonstrated the movement of the aortic cusps (Fig. 7*E*) and the changing diameter of the ascending aorta through the cardiac cycle (Fig. 7*G*).

The left coronary artery was imaged in a left parasternal transverse section (LT3) (Fig. 8*A*). The Doppler flow spectrum recorded from the proximal part of the left coronary artery revealed a continuous and pulsatile flow pattern through the cardiac cycle (Fig. 8*B*).

The entire aortic arch and its three branches were well visualized only in a right parasternal longitudinal section pointed leftward and with sharp angle to the coronal plane (RL4) (Fig. 9*A*). The innominate artery and the succeeding right common carotid artery were imaged by a right parasternal longitudinal section (RL3) (Fig. 9*C*). The left common carotid artery was imaged in its long axis by a left parasternal longitudinal section (LL1a) (Fig. 9*D*). Both common carotid arteries could be followed up to their bifurcations. The proximal left subclavian artery and left superior vena cava were visualized in another left parasternal longitudinal section parallel to LL1a (LL1b) (Fig. 9*E*).

M-mode cardiac dimension measurements are presented in Table 2. No significant difference was found in the measured left ventricular dimension between the long-axis view and short-axis view nor in the measured aortic diameter between the left and right parasternal longitudinal sections. The end-systolic aortic diameter is larger than the end-diastolic diameter by, on average, 15% in left parasternal section and 18% in right parasternal section. The cardiac Doppler flow measurements are presented in Table 3, and significant differences in the Doppler flow patterns were found between the right and left sides of the heart at all three anatomical levels.

DISCUSSION

This study presents a comprehensive protocol for transthoracic cardiac imaging in adult mice using 30 MHz ultrasound. The thoracic gross anatomy related to ultrasound cardiac imaging was verified with MR imaging. Three important acoustic windows, the right parasternal, left parasternal, and apical windows, are identified. From each window, a series of ultrasound imaging sections were employed for observing the cardiac structures using 2D imaging, the ventricular dimension

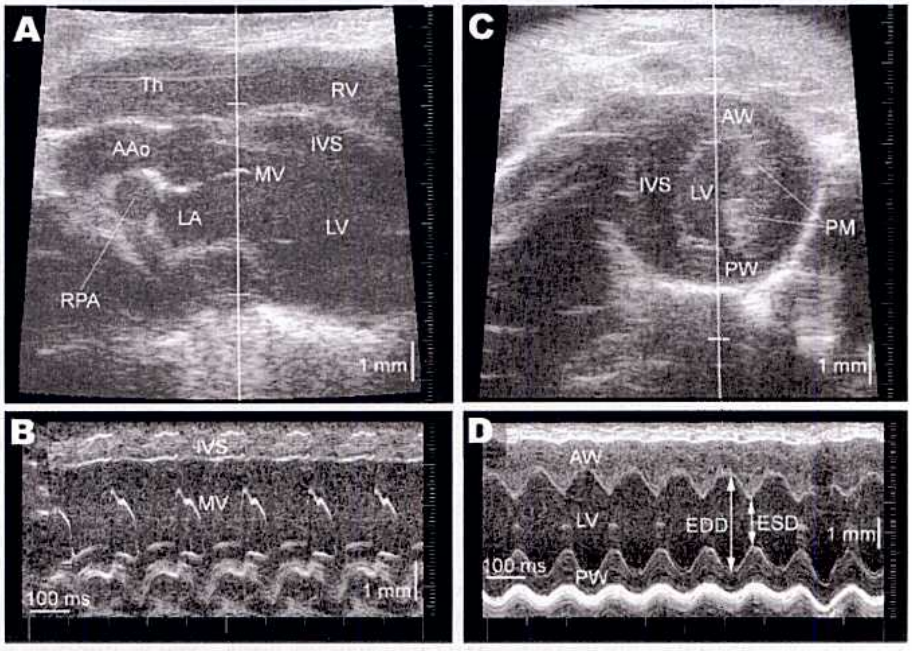

Fig. 5. M-mode recordings of the MV and LV. *A*: 2D image of a right parasternal longitudinal section (RL5) showing the MO and MV, as well as the AO and AAo. The M-mode cursor line is located over the MV. *B*: M-mode recording of the anterior leaflet of MV showing the double peaks during diastolic opening. *C*: 2D image of a left parasternal transverse section (LT4) showing the LV in short axis, with M-mode cursor line through its largest dimension. *D*: M-mode recording of the LV. AW, anterior wall of left ventricle; EDD, end-diastolic diameter; ESD, end-systolic diameter; IVS, inter-ventricular septum; PM, papillary muscle; PW, posterior wall of left ventricle. Refer to the legends of Figs. 1–4 for definitions of other abbreviations.

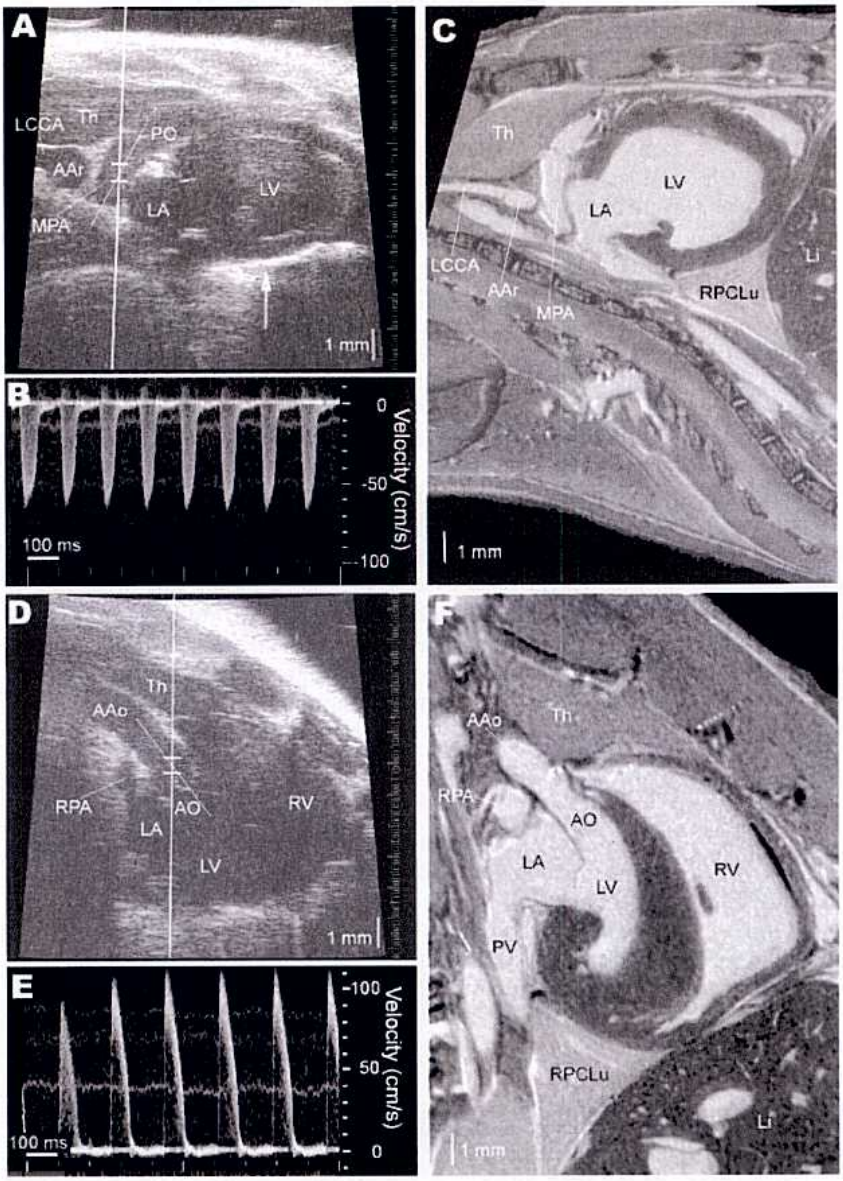

Fig. 6. UBM imaging of the right and left ventricular outflow tracts, with anatomical confirmation by MR imaging. *A*: UBM image of a left parasternal longitudinal section (LL3) showing the MPA, with the Doppler sample volume distal to the pulmonary orifice (PO). Arrow indicates the bright reverberations at the interface exiting the myocardium into lung. *B*: Doppler spectrum recorded from MPA. *C*: MR image at the similar section as for UBM image in *A*, showing the MPA and its spatial relation with surrounding structures such as LA, Th, and AAr. *D*: UBM image of an upper right parasternal longitudinal section (RL1) showing the AAo in its longitudinal axis with Doppler sample volume at the level just distal to AO. *E*: Doppler flow velocity spectrum recorded from AAo. *F*: MR image of a similar section as for the UBM image in *D*. LCCA, left common carotid artery. Refer to the legends of Figs. 1–5 for definitions of other abbreviations.

and function by M-mode recording, and the hemodynamics by Doppler flow sampling. Observation was focused on the most important parts of the mouse heart as follows: *1*) the right atrial inflow channels, *2*) the right ventricular inflow tract, *3*) the right ventricular outflow tract, *4*) the left atrial inflow channel, *5*) the left ventricular inflow tract, *6*) the left ventricular outflow tract, *7*) the left coronary artery, and *8*) the aortic arch and its three branches. Left ventricular and aortic dimensions were measured. Doppler flow velocity spectra were recorded from six intracardiac locations: right superior vena cava, tricuspid orifice, main pulmonary artery, pulmonary vein, mitral orifice, and ascending aorta.

Characteristics of Transthoracic Acoustic Windows and Ultrasound Cardiac Imaging Sections in Mice

MR data shows that mouse thoracic anatomy is very different from humans. In human adults, the lung lobes present from the top of the thoracic cavity (close to the level of the clavicle) to the diaphragm on both sides. Most of the human heart (especially the right side) and the associated great vessels are encompassed by the lung lobes. The sternum of human adult is flat and relatively wide, and the thymus is small with the remnants in the anterior mediastinal fat (10). For all these reasons, an acoustical window is not available at all on the right side of the sternum in humans (32). In mice, the posto-inferior location of the lung lobes relative to heart (8), the narrow sternum, and the relatively large thymus (which is hypoechogenic in ultrasound imaging) result in large parasternal acoustic windows on both right and left sides of the sternum for transthoracic cardiac imaging.

One of the benefits of these anatomical features in mice is that all ascending aorta, entire aortic arch, and its three branches can be visualized from both right and left parasternal windows. Both left and right common carotid arteries can be followed up to their bifurcations (35). This advantage

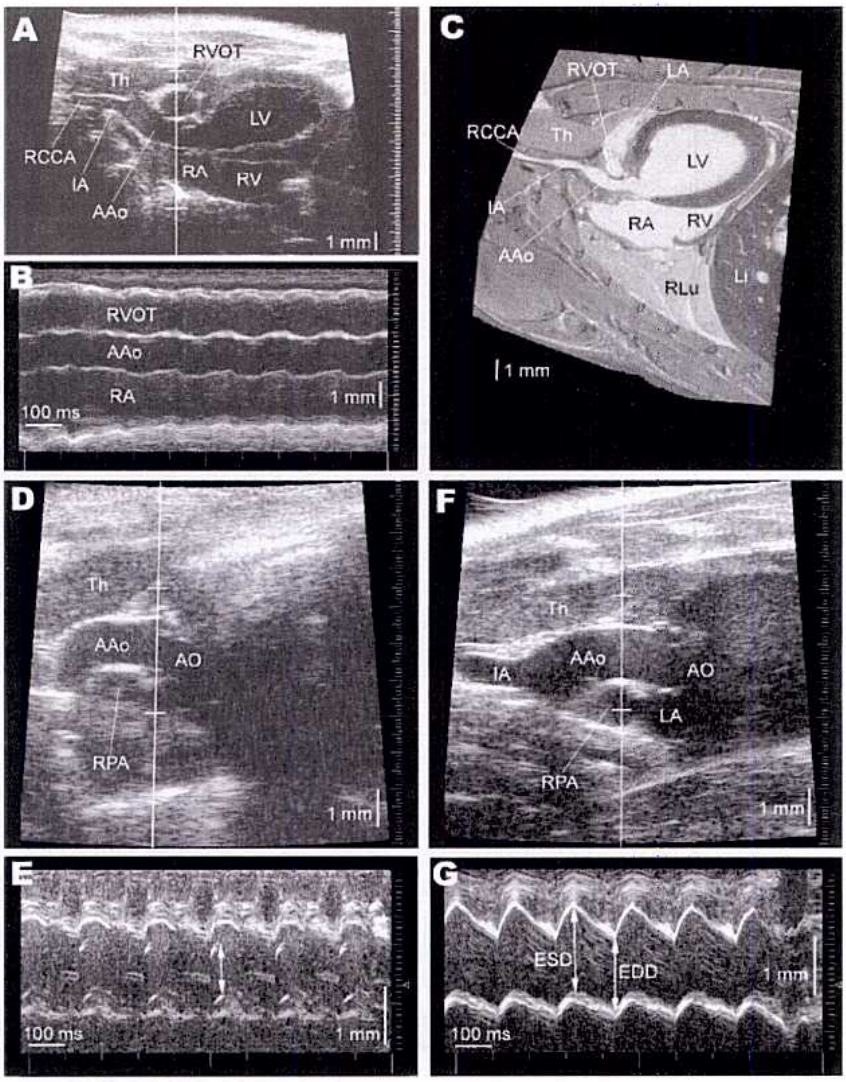

Fig. 7. UBM imaging of the left ventricular outflow tract and AAo, with anatomical confirmation from MR imaging. *A*: UBM image of a left parasternal longitudinal section (LL2) showing the left ventricular outflow tract and AAo, as well as the RA and RV in the far field and the RVOT in the near field. *B*: M-mode recording simultaneously demonstrates the dimensional changes of RVOT, AAo, and RA through cardiac cycles. *C*: MR image of the similar section as for the UBM image in *A*. *D*: UBM image of a right parasternal longitudinal section (RL5) showing the AO and AAo, with M-mode cursor line across the aortic cusps. *E*: M-mode recording at the level of the AO showing the movement of the aortic cusps. The arrow indicates the opening of the aortic cusps during systole. *F*: UBM image of a right parasternal longitudinal section (RL5) showing the AO and AAo, but with the M-mode cursor line at the level of AAo. *G*: M-mode recording of the AAo showing the overall excursion and dimension changes through cardiac cycle. IA, innominate artery. RCCA, right common carotid artery. Refer to the legends of Figs. 1–6 for definitions of other abbreviations.

is very important for phenotyping the atherosclerotic models such as LDLR and ApoE knockout mice in which the atherosclerotic plaques often occur in aortic sinuses, along the lesser curvature of the aortic arch, and in innominate artery and the proximal part of common carotid arteries (9, 27). The morphology, distribution, of the atherosclerotic plaques and their effect on flow dynamics can be observed longitudinally with the progress of disease.

The MR data also demonstrate that the mouse aortic orifice and ascending aorta are located on the right side of the midline of the chest, and the mitral orifice is located relatively leftward and posteriorly. Therefore, the right parasternal window is the only approach to simultaneously visualize both aortic and mitral orifices in a single imaging section. In this right parasternal longitudinal section, the mitral leaflets are clearer than in any other sections and the M-mode tracing of the valvular movement is optimal, probably due to the perpendicular relation between the ultrasound beam and the surface of mitral leaflets (Fig. 5, *A* and *B*). In this aspect, mice are different from humans, where a left parasternal longitudinal section is needed to visualize both the left ventricular inflow tract and outflow tract in the same view (32), because these structures are mostly on the left side of the midline in humans (10). In mice, however, the similar section from the left parasternal window used to view the left ventricular outflow tract and the ascending aorta simultaneously demonstrates the right atrium and ventricle in the far field of the image (rather than the left atrium and ventricle as in humans). We recommend that this section (LL2) be used as a standard view for evaluating the relative chamber size of right heart compared with that of left heart, in 2D imaging and M-mode recording (Fig. 7, *A–C*).

The right parasternal window also provides the shortest approach for observing the aortic orifice and ascending aorta. The recording of aortic valvular movement is helpful in characterizing mouse models with aortic valvular abnormalities (20). Aortic diameters measured from the left and right parasternal windows are not significantly different. However, averaging the results from these two almost orthogonal planes will further improve the accuracy of aortic diameter measurement for flow volume calculation, without any need of assuming the circular shape of the ascending aorta.

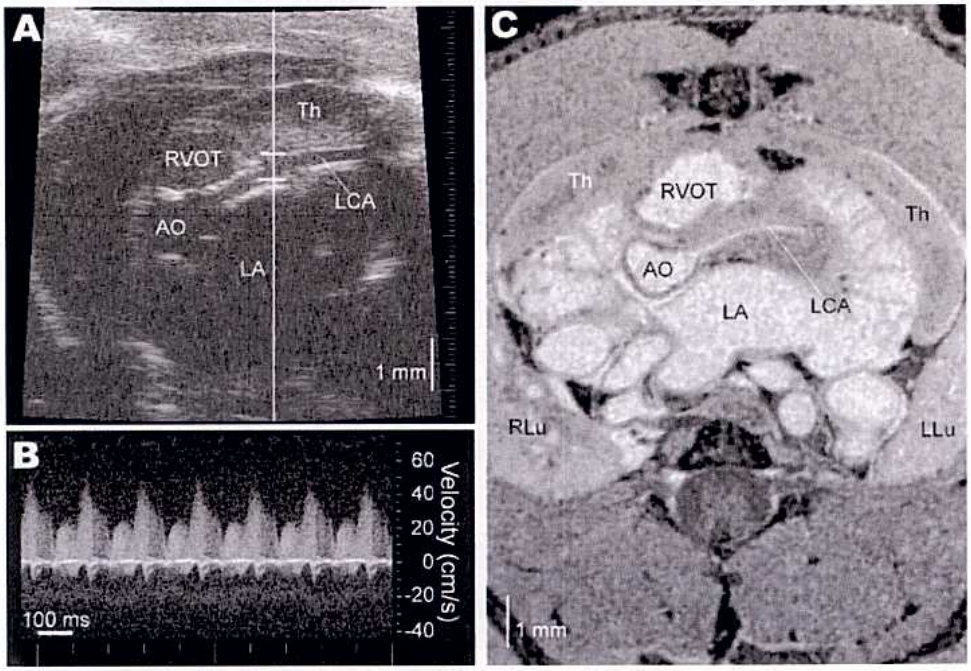

Fig. 8. UBM imaging of the left coronary artery (LCA), with anatomical confirmation by MR imaging. *A*: UBM image of a left parasternal transverse section (LT3) showing the proximal part of LCA. *B*: Doppler flow spectrum recorded from LCA showing the continuous and pulsatile waveforms. *C*: MR image of the similar section as for the UBM image in *A*. Refer to the legends of Figs. 1–7 for definitions of other abbreviations.

Cardiovascular Phenotyping Using High-Frequency Ultrasound Imaging in Mice

Comprehensive cardiovascular phenotyping in mice should include observations of morphology, function, and hemodynamics throughout the whole cardiovascular system but not just be limited to the left ventricle and aorta as in most previous studies. Mice with hypoxia and pulmonary hypertension develop right ventricular hypertrophy (29), whereas others with congenital cardiac malformations such as Tbx5 mutants (4) demonstrate morphological abnormalities of right cardiac chambers. In atherosclerotic mice the lesions involve in the great arteries and coronary artery and result in myocardial infarction, abnormal ventricular wall motion, and systolic dysfunction (3, 9, 27).

The mouse cardiac gross morphology can observed with much higher spatial resolution than ever before. Because of the irregular shape of the left and right atria and right ventricle, certain imaging sections have to be selected as standard for dimension measurement so that the data obtained from different mouse groups or from different time points in a serial study are comparable. The size of the left atrium can be evaluated in the left parasternal longitudinal view of the left ventricular inflow tract (Fig. 3*D*) and the apical four-chamber view (Fig. 4*D*). The dimensions of the right atrium and right ventricle can be evaluated in the left parasternal longitudinal view in which the right heart is demonstrated in contrast to the left ventricular outflow tract and ascending aorta (Fig. 7*A*).

This study presents a systematic methodology for in vivo functional evaluation. The left ventricular systolic function can be evaluated based on the parameters derived from M-mode dimension measurements (7). Doppler flow spectra obtained from the ascending aorta can be used for measuring the parameters such as the peak flow velocity, rising time, peak acceleration rate, and ejection time to assess the left ventricular systolic function (13). Accordingly, the pulmonary arterial Doppler flow spectrum as obtained in this study can be used to evaluate the right ventricular systolic function in a similar way.

We also demonstrate a novel way of measuring the aortic flow velocity in mice. From the upper right parasternal window, the entire ascending aorta can be visualized with a small intercept angle between the Doppler beam and the long axis of aorta, and the aortic velocity can be measured exactly from any desired site. The aortic peak velocity in our study is higher than those (50~75 cm/s) measured from apical four-chamber view in previous studies (15, 25, 31) but similar to those measured with a small pure Doppler probe from the suprasternal notch (90 ± 11 cm/s), where the incidence angle between the ultrasound beam and ascending aorta was assumed to be close to zero (13).

We have further confirmed the specific flow patterns in the mitral and tricuspid orifices as previously found in mice of a different strain (36). Doppler ventricular inflow pattern is used to evaluate the ventricular diastolic function in humans, and it has been suggested that the ventricular diastolic dysfunction precedes the systolic dysfunction in various cardiac diseases (23). Abnormal left ventricular diastolic filling patterns were also observed in phospholamban-deficient mice (15) and hyperthyroid mice (30). However, in a situation called "pseudonormalization" of the left ventricular inflow pattern in humans, the mitral Doppler flow pattern becomes normal when the left atrial pressure gradually increases with the progress of disease, then the left ventricular diastolic dysfunction can only be reflected in the pattern of the pulmonary venous flow (26). The abnormal flow pattern in vena cava and pulmonary vein can also be detected in many disease conditions with elevated atrial pressure in humans (23, 26). Therefore, simultaneous observation on the atrial inflow and ventricular inflow will provide much more insight into the dynamics of ventricular filling in mice modeling human diseases such as constrictive pericarditis and tamponade.

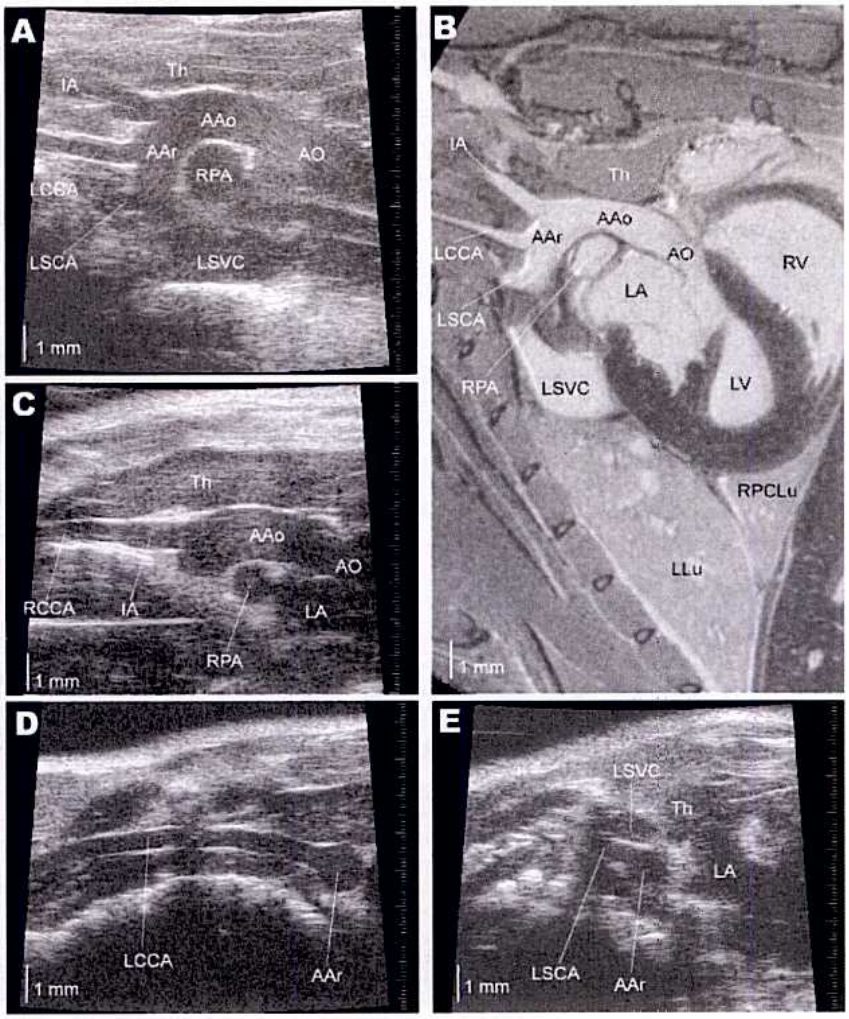

Fig. 9. UBM imaging of the entire AAr and its associate branches, with anatomical confirmation by MR imaging. *A*: UBM image of a right parasternal longitudinal section (RL4) showing the AAo, entire AAr, and the proximal parts of its three branches, i.e., IA, LCCA, and left subclavian artery (LSCA). *B*: MR image of the similar section as for the UBM image in *A*. *C*: UBM image of a right parasternal longitudinal section (RL3) showing the AAo, IA, and RCCA. *D*: UBM image of a left parasternal longitudinal section (LL1a) showing the AAr in short axis and the LCCA in longitudinal axis. *E*: UBM image of a left parasternal longitudinal section (LL1b) showing the AAr in short axis and the proximal LSCA and LSVC. Refer to the legends of Figs. 1–8 for definitions of other abbreviations.

The present study for the first time presents reliable methods of recording Doppler flow spectra from the superior vena cava and pulmonary vein in mice. The lower D wave in the superior vena cava corresponds well to the lower E wave in the tricuspid orifice, and the higher D wave in the pulmonary vein is consistent with the higher E wave in the mitral orifice. These results suggest that during diastole the right ventricular active relaxation makes less contribution to ventricular filling, whereas the left ventricular active relaxation plays a dominant role in ventricular filling. These findings in mice are different from those in adult humans where the inflow patterns are similar on both sides of the heart. In humans, the S wave is usually higher than the D wave in both vena cava and pulmonary vein, and the E wave is always higher than the A wave in both tricuspid and mitral orifices (23). The underlying mechanisms responsible for the difference in ventricular diastolic filling pattern between right and left sides of the heart in mice, and the differences between mice and humans, need to be further explored.

Although UBM has greatly advanced cardiac evaluation in mice, there are still limitations in the present implementations. Reduction in transducer size and increase in sector angle will allow for additional transthoracic approaches and imaging sections. The frame rate of 2D imaging was not high enough

Table 2. *Cardiac dimensions measured from M-mode recording*

Parameters	Units	Measurements	
		LV (LAV)	*LV (SAV)*
Heart rate	beats/min	429±19	429±18
End-diastole			
AW	mm	0.86±0.03	0.84±0.03
EDD	mm	3.84±0.09	3.80±0.07
PW	mm	0.74±0.02	0.75±0.03
End-systole			
AW	mm	1.36±0.07	1.34±0.06
ESD	mm	2.45±0.09	2.44±0.08
PW	mm	1.08±0.04	1.07±0.04
PW velocity	mm/s	18.6±1.0	17.9±1.0
		AAo (left parasternal)	*AAo (right parasternal)*
Heart rate	beats/min	404±16	407±20
ESD	mm	1.37±0.02	1.36±0.04
EDD	mm	1.18±0.01	1.14±0.04

Values are means ± SE; n = 12; AW, anterior wall of left ventricle; EDD, end-diastolic diameter; ESD, end-systolic diameter; LAV, long-axis view; PW, posterior wall of left ventricle; SAV, short-axis view. Refer to legend of Table 1 for definitions of other acronyms. No significant difference was found in the corresponding parameters of left ventricular dimensions between the long- and short-axis views nor in the aortic diameter between the left and right parasternal longitudinal views. The paired Student's *t*-test was used for comparison.

Table 3. *Cardiac hemodynamic parameters measured by pulsed Doppler and the comparison of flow patterns between the right and left sides of the heart*

Parameters	Units	Right Side of Heart	Left Side of Heart	*P* Value (paired *t*-test)
		RSVC (n = 12)	*PV (n = 12)*	
Incidence angle	degree	33±3	21±3	
Heart rate	beats/min	381±11	441±16	
Doppler waveform				
Peak S	cm/s	19±2	20±1	NS
Peak D	cm/s	12±1	54±4	<0.01
Peak A	cm/s	6±1	4±1	NS
		TO (n = 8)*	*MO (n = 8*)*	
Intercept angle	degree	16±4	9±2	
Heart rate	beats/min	389±22	405±18	
Doppler waveform				
Peak E	cm/s	28±1	60±2	<0.01
Peak A	cm/s	38±1	39±2	NS
Peak E/A ratio		0.73±0.04	1.58±0.07	<0.01
		MPA (n = 12)	*AAo (n = 12)*	
Intercept angle	degree	12±2	33±2	
Heart rate	beats/min	435±16	381±16	
Doppler waveform				
PFV	cm/s	66±2	105±2	<0.01
TVI	cm	2.9±0.1	4.4±0.1	<0.01

Values are means ± SE. *Peak A* is the peak velocity of the late diastolic filling wave (A wave) of mitral and tricuspid Doppler flow spectra, or the peak velocity of the late diastolic retrograde wave (A wave) due to the atrial contraction in the Doppler flow spectra of superior vena cava and pulmonary vein. *Peak E* is the peak velocity of the early diastolic filling wave (E wave) of mitral and tricuspid Doppler flow spectra. *Peak E/A* is the ratio of *peak E* to *peak A* of mitral or tricuspid Doppler flow spectrum. *Peak S* is the peak velocity of the systolic wave (S wave) of the Doppler flow spectrum of the superior vena cava or pulmonary vein. *Peak D* is the peak velocity of the early diastolic wave (D wave) of the Doppler flow spectrum of the superior vena cava or pulmonary vein. PFV, peak flow velocity; TVI, time-velocity integral of Doppler spectrum. Refer to the legend of Table 1 for definitions of other acronyms. *In the Doppler flow measurement of tricuspid and mitral orifices, four cases were excluded from analysis because the E and A waves did not separate due to high heart rate. NS, not significantly different.

relative to the heart rate of adult mice. Given an average heart rate of 400 beats/min in present data, there were just 4.5 frames per cardiac cycle, and it was thus inaccurate in identifying the image frames of end-systole and end-diastole for functional evaluation. Therefore, in this study we used the 2D imaging just for observing the cardiac gross morphology and individual structures and for guiding the M-mode recording and Doppler flow velocity sampling. All quantitative dimension measurements were obtained from M-mode recording. In the 30-MHz frequency range, it is not yet technologically feasible to employ a linear array transducer to achieve the required 100–500 Hz frame rate for the quantitative 2D imaging of the mouse heart. In addition, simultaneous ECG recording needs to be integrated with M-mode and Doppler mode for more comprehensive analysis.

Anesthesia may cause the decrease of heart rate and depression of cardiac function, but it is needed to immobilize mice for data acquisition. Compared with other commonly used anesthetics, isoflurane has the least effect on heart rate and cardiac function (15, 25, 38). This issue has been discussed in details in our previous study (36). In this study, mice were under anesthesia for relatively long time (45–60 min), and the decrease and variation in the heart rate (range 380–440 beats/min) were observed throughout the experiment. Therefore, the quantitative M-mode and Doppler measurements presented in this paper should not be simply taken as normal physiological values. Once more experience has been obtained in mouse cardiac imaging, future studies with more limited objectives will take shorter time, and such limitations can be minimized.

Although the results in this study were from young adult mice, the established methodology was also applied to a group of relatively older mice (17 wk, body wt 25–27 g) in a recent study in our laboratory. MR images of those mice demonstrated very similar thoracic anatomy, e.g., the posto-inferior location of the lung lobes relative to the heart and the narrow sternum. The thymus in the older mice looked smaller than that of the younger mice in the present paper, but it was still laterally wider than the sternum. In ultrasound imaging of those older adult mice, all acoustic windows and imaging sections were available, and the functional and hemodynamic measurements were feasible as described in this paper.

Conclusions

This study for the first time presents a systematic protocol for comprehensive in vivo trans-thoracic cardiac imaging using high-frequency ultrasound on mice. Three major acoustical windows are located. A series of sections are identified for evaluating the cardiac morphology using 2D imaging, the ventricular function using M-mode recording, and the hemodynamics using Doppler flow sampling. The thoracic gross anatomy related to trans-thoracic ultrasound cardiac imaging is elucidated based on the whole body MR imaging, and the individual cardiac structures in 2D ultrasound images are verified by comparing with the similar sections of the 3D MR data set. Critical measurements such as ventricular and aortic dimensions and the flow velocities at the representative intracardiac locations are provided. All these fundamental methodologies and preliminary data are very important for the extensive applications of high-frequency ultrasound imaging in the cardiovascular morphological and functional phenotyping of mutant mice in the future.

ACKNOWLEDGMENTS

We thank Jun Dazai for technical support, and we thank Dr. Natasa Kovacevic and Leila Baghdadi for help in data processing and analysis. We also thank Dr. S. Lee Adamson for help with the study and manuscript.

GRANTS

This work is part of the Mouse Imaging Centre at the Hospital for Sick Children and the University of Toronto. The infrastructure has been funded by the Canada Foundation for Innovation and Ontario Innovation Trust. The research has been funded by an Ontario Research and Development Challenge Fund grant to the Ontario Consortium for Small Animal Imaging.

DISCLOSURES

F. S. Foster acknowledges a financial interest in VisualSonics, Inc. Y.-Q. Zhou consults for VisualSonics, Inc.

REFERENCES

1. **Balaban RS and Hampshire VA.** Challenges in small animal noninvasive imaging. *ILAR J* 42: 248–262, 2001.
2. **Bock NA, Konyer NB, and Henkelman RM.** Multiple-mouse MRI. *Magn Reson Med* 49: 158–67, 2003.
3. **Braun A, Trigatti BL, Post MJ, Sato K, Simons M, Edelberg JM, Rosenberg RD, Schrenzel M, and Krieger M.** Loss of SR-BI expression leads to the early onset of occlusive atherosclerotic coronary artery

disease, spontaneous myocardial infarctions, severe cardiac dysfunction, and premature death in apolipoprotein E-deficient mice. *Circ Res* 90: 270–276, 2002.

4. **Bruneau BG, Nemer G, Schmitt JP, Charron F, Robitaille L, Caron S, Conner DA, Gessler M, Nemer M, Seidman CE, and Seidman JG.** A murine model of Holt-Oram syndrome defines roles of the T-box transcription factor Tbx5 in cardiogenesis and disease. *Cell* 106: 709–721, 2001.
5. **Coatney RW.** Ultrasound imaging: principles and applications in rodent research. *ILAR J* 42: 233–247, 2001.
6. **Collins KA, Korcarz CE, Shroff SG, Bednarz JE, Fentzke RC, Lin H, Leiden JM, and Lang RM.** Accuracy of echocardiographic estimates of left ventricular mass in mice. *Am J Physiol Heart Circ Physiol* 280: H1954–H1962, 2001.
7. **Collins KA, Korcarz CE, and Lang RM.** Use of echocardiography for the phenotypic assessment of genetically altered mice. *Physiol Genomics* 13: 227–239, 2003; 10.1152/physiolgenomics.00005.2003.
8. **Cook MJ.** *The Anatomy of the Laboratory Mouse*. London: Academic, 1965, p. 101–112.
9. **Daugherty A.** Mouse models of atherosclerosis. *Am J Med Sci* 323: 3–10, 2002.
10. **Ellis H, Logan BM, and Dixon AK.** *Human Sectional Anatomy-Atlas of Body Sections, CT and MRI Images*. Oxford: Butterworth-Heinemann, 1999, p. 97–122.
11. **Fatkin D, Christe ME, Aristizabal O, McConnell BK, Srinivasan S, Schoen FJ, Seidman CE, Turnbull DH, and Seidman JG.** Neonatal cardiomyopathy in mice homozygous for the Arg403Gln mutation in the alpha cardiac myosin heavy chain gene. *J Clin Invest* 103: 147–153, 1999.
12. **Foster FS, Pavlin CJ, Harasiewicz KA, Christopher DA, and Turnbull DH.** Advances in ultrasound biomicroscopy. *Ultrasound Med Biol* 26: 1–27, 2000.
13. **Hartley CJ, Michael LH, and Entman ML.** Noninvasive measurement of ascending aortic blood velocity in mice. *Am J Physiol Heart Circ Physiol* 268: H499–H505, 1995.
14. **Hoffman JM and Croft BY.** Future directions in small animal imaging. *Lab Anim (NY)* 30: 32–35, 2001.
15. **Hoit BD, Khoury SF, Kranias EG, Ball N, and Walsh RA.** In vivo echocardiographic detection of enhanced left ventricular function in gene-targeted mice with phospholamban deficiency. *Circ Res* 77: 632–637, 1995.
16. **Hoit BD.** New approaches to phenotypic analysis in adult mice. *J Mol Cell Cardiol* 33: 27–35, 2001.
17. **Johnson GA, Turnbull DH, and Fitzsimons EG (Editors).** In Vivo *Microscopy: Technologies and Applications. A Workshop for Small Animal Imaging* [Online]. Gaithersburg, MD: March 18–19, 1999. http://www.ncrr.nih.gov/biotech/invivomicro03–1999.pdf.
18. **Johnson GA, Cofer GP, Gewalt SL, and Hedlund LW.** Morphologic phenotyping with MR microscopy: the visible mouse. *Radiology* 222: 789–793, 2002.
19. **Johnson GA, Cofer GP, Fubara B, Gewalt SL, Hedlund LW, and Maronpot RR.** Magnetic resonance histology for morphologic phenotyping. *J Magn Reson Imaging* 16: 423–429, 2002.
20. **Lee TC, Zhao YD, Courtman DW, and Stewart DJ.** Abnormal aortic valve development in mice lacking endothelial nitric oxide synthase. *Circulation* 101: 2345–2348, 2000.
21. **Liao Y, Ishikura F, Beppu S, Asakura M, Takashima S, Asanuma H, Sanada S, Kim J, Ogita H, Kuzuya T, Node K, Kitakaze M, and Hori M.** Echocardiographic assessment of LV hypertrophy and function in aortic-banded mice: necropsy validation. *Am J Physiol Heart Circ Physiol* 282: H1703–H1708, 2002. First published December 13, 2001; 10.1152/ajpheart.00238.2001.
22. **McConnell BK, Jones KA, Fatkin D, Arroyo LH, Lee RT, Aristizabal O, Turnbull DH, Georgakopoulos D, Kass D, Bond M, Niimura H, Schoen FJ, Conner D, Fischman DA, Seidman CE, and Seidman JG.** Dilated cardiomyopathy in homozygous myosin-binding protein-C mutant mice. *J Clin Invest* 104: 1235–1244, 1999.
23. **Nishimura RA, Abel MD, Hatle LK, and Tajik AJ.** Assessment of diastolic function of the heart: background and current applications of Doppler echocardiography. Part II. Clinical studies. *Mayo Clin Proc* 64: 181–204, 1989.
24. **Paulus MJ, Gleason SS, Easterly ME, and Foltz CJ.** A review of high-resolution X-ray computed tomography and other imaging modalities for small animal research. *Lab Anim (NY)* 30: 36–45, 2001.
25. **Pollick C, Hale SL, and Kloner RA.** Echocardiographic and cardiac Doppler assessment of mice. *J Am Soc Echocardiogr* 8: 602–610, 1995.
26. **Quinones MA, Otto CM, Stoddard M, Waggoner A, and Zoghbi WA.** Recommendations for quantification of Doppler echocardiography: a report from the Doppler Quantification Task Force of the Nomenclature and Standards Committee of the American Society of Echocardiography. *J Am Soc Echocardiogr* 15: 167–184, 2002.
27. **Rosenfeld ME, Polinsky P, Virmani R, Kauser K, Rubanyi G, and Schwartz SM.** Advanced atherosclerotic lesions in the innominate artery of the ApoE knockout mouse. *Arterioscler Thromb Vasc Biol* 20: 2587–92, 2000.
28. **Sahn DJ, DeMaria A, Kisslo J, and Weyman A.** Recommendations regarding quantitation in M-mode echocardiography: results of a survey of echocardiographic methods. *Circulation* 58: 1072–1083, 1978.
29. **Scherrer-Crosbie M, Steudel W, Hunziker PR, Foster GP, Garrido L, Liel-Cohen N, Zapol WM, and Picard MH.** Determination of right ventricular structure and function in normoxic and hypoxic mice: a transesophageal echocardiographic study. *Circulation* 98: 1015–1021, 1998.
30. **Taffet GE, Hartley CJ, Wen X, Pham T, Michael LH, and Entman ML.** Noninvasive indexes of cardiac systolic and diastolic function in hyperthyroid and senescent mouse. *Am J Physiol Heart Circ Physiol* 270: H2204–H2209, 1996.
31. **Tanaka N, Dalton N, Mao L, Rockman HA, Peterson KL, Gottshall KR, Hunter JJ, Chien KR, and Ross J Jr.** Transthoracic echocardiography in models of cardiac disease in the mouse. *Circulation* 94: 1109–1117, 1996.
32. **Weyman AE.** *Principles and Practice of Echocardiography*. Philadelphia: Lea and Febiger, 1994, p. 75–123.
33. **Wong WH and Sukumar S.** "Millipede" imaging coil design for high field micro imaging applications (Abstract). *Proc ISMRM 8th Annu Meet Denver, Apr 1–7, 2000*, p. 1399.
34. **Yang XP, Liu YH, Rhaleb NE, Kurihara N, Kim HE, and Carretero OA.** Echocardiographic assessment of cardiac function in conscious and anesthetized mice. *Am J Physiol Heart Circ Physiol* 277: H1967–H1974, 1999.
35. **Zhou YQ, Foster FS, Qu DW, Zhang M, Harasiewicz KA, and Adamson SL.** Applications for multifrequency ultrasound biomicroscopy in mice from implantation to adulthood. *Physiol Genomics* 10: 113–126, 2002. First published June 18, 2002; 10.1152/physiolgenomics.00119.2001.
36. **Zhou YQ, Foster FS, Parkes R, and Adamson SL.** Developmental changes in left and right ventricular diastolic filling patterns in mice. *Am J Physiol Heart Circ Physiol* 285: H1563–H1575, 2003. First published June 12, 2003; 10.1152/ajpheart.00384.2003.
37. **Zhou YQ, Davidson L, Henkelman RM, Nieman BJ, Foster FS, Yu LX, and Chen XJ.** Ultrasound-guided left ventricular catheterization: A novel method of whole mouse perfusion for microimaging. *Lab Invest* 84:385–389, 2004.
38. **Zuurbier CJ, Emons VM, and Ince C.** Hemodynamics of anesthetized ventilated mouse models: aspects of anesthetics, fluid support, and strain. *Am J Physiol Heart Circ Physiol* 282: H2099–H2105, 2002. First published February 14, 2002; 10.1152/ajpheart.01002.2001.